

CHANDRA OBSERVATIONS OF THE QSO PAIR Q2345+007:
BINARY QUASAR OR MASSIVE DARK LENS?

PAUL J. GREEN^{1,2}, CHRIS KOCHANÉK, ANETA SIEMIGINOWSKA, DONG-WOO KIM, MAXIM
MARKEVITCH, JOHN SILVERMAN¹, ANIL DOSAJ¹,

Harvard-Smithsonian Center for Astrophysics, 60 Garden St., Cambridge, MA 02138

BUELL T. JANNUZI¹

National Optical Astronomy Observatory, P.O. Box 26732, Tucson, AZ 85726-6732

CHRIS SMITH¹

Cerro Tololo Inter-American Observatory, National Optical Astronomy Observatory, Casilla 603, La Serena,
Chile.

ApJ, accepted Feb 1, 2002

ABSTRACT

The components of the wide ($7''.3$) separation quasar pair Q2345+007A,B ($z = 2.15$) have the most strikingly similar optical spectra seen to date (Steidel & Sargent 1991) yet no detected lensing mass, making this system the best candidate known for a massive ($\sim 10^{14}M_{\odot}$) dark matter lens system. Here we present results from a 65 ksec *Chandra* observation designed to investigate whether it is a binary quasar or a gravitational lens. We find no X-ray evidence for a lensing cluster to a (0.5-2keV) flux limit of $2 \times 10^{-15} \text{erg cm}^{-2} \text{s}^{-1}$, which is consistent with lensing only for a reduced baryon fraction. Using the *Chandra* X-ray observations of the quasars themselves, together with new and published optical measurements, we use the observed emission properties of the quasars for further tests between the lens and binary hypotheses. Assuming similar line-of-sight absorption to the images, we find that their X-ray continuum slopes are inconsistent ($\Gamma_A = 2.30_{-0.30}^{+0.36}$ and $\Gamma_B = 0.83_{-0.44}^{+0.49}$) as are their X-ray to optical flux ratios. The probability that B suffers absorption sufficient to account for these spectral differences is negligible. We present new optical evidence that the flux ratio of the pair is variable, so the time-delay in a lens scenario could cause some of the discrepancies. However, adequately large variations in overall spectral energy distribution are rare in individual QSOs. All new evidence here weighs strongly toward the binary interpretation. Q2345+007 thus may represent the highest redshift example known of interaction-triggered but as-yet unmerged luminous AGN.

Subject headings: gravitational lensing – quasars: absorption lines – quasars: individual (Q2345+007) – X-rays: general – X-rays: individual (Q2345+007)

1. INTRODUCTION

The density and evolution of massive halos ($M > 10^{14}M_{\odot}$) is a powerful probe of the cosmological model. The number of massive clusters depends exponentially on the amplitude of the power spectrum when normalized by σ_8 , the amplitude on a scale of $8h^{-1}$ Mpc. These halos can be detected through an overdensity of galaxies (e.g. Postman et al. 1996 for a modern example), from X-ray emission (e.g. Ebeling et al. 2000), or with the Sunyaev-Zeldovich effect (e.g. Holder et al. 2000). All these methods depend on emission or absorption from the baryons in the halo. Alternatively, we can detect such massive halos using gravitational lensing. This can be done either with weak lensing surveys (Wittman et al. 2001) or surveys for multiply imaged background sources with wide image separations (usually defined by $\Delta\theta > 3''$; Kochanek, Falco & Munoz 1999, hereafter KFM99).

Unlike the other methods of finding clusters, gravitational lensing can also find “dark” clusters where there

is mass but no detectable baryons. Some candidates have been found in weak lensing (shear-selected) surveys (Umetsu & Futamase 2000; Erben et al. 2000), but only one such cluster has been spectroscopically confirmed to date (Wittman et al. 2001). Most of the debate about dark halos has focused on the population of wide-separation quasar pairs (WSQPs). All the lens candidates with separations $\Delta\theta < 3''$ have identifiable primary lens galaxies in deep NICMOS observations (see synopses in KFM99, or Mortlock & Webster 2000). Above $3''$ there are 17 objects. Four are *bona fide* gravitational lenses, with similar optical/radio flux ratios and negligible spectroscopic differences, as well as a plausible lensing galaxy. Eight more pairs, with discrepant radio/optical flux ratios for a lens, or $> 3\sigma$ velocity differences, are very probably binary quasars. The remaining 5 objects are WSQPs with similar spectra, essentially identical redshifts, and no visible lens galaxy or cluster. Were four pairs found to be dark clusters, they would imply that the dark clusters

¹ Visiting Astronomer, Kitt Peak National Observatory and/or Cerro Tololo Inter-American Observatory, National Optical Astronomy Observatory, operated by the Association of Universities for Research in Astronomy, Inc. (AURA) under cooperative agreement with the National Science Foundation.

² email: pgreen@cfa.harvard.edu

were just as numerous as normal clusters.

The problem with simply interpreting the WSQPs as dark clusters is that we expect to find WSQPs even in the absence of dark lensing as examples of binary quasars in which the central engines of two nearby galaxies are simultaneously active. We know that many of the pairs are binary quasars because they have discrepant flux ratios as a function of wavelength or $> 3\sigma$ velocity differences. We can prove from statistical analyses of the relative numbers of radio-quiet/radio-quiet, radio-quiet/radio-loud and radio-loud/radio-loud pairs that most of the remaining WSQPs are binary quasars (KFM99). Since the number of WSQPs is 100 times higher than expected from simple extrapolations of the quasar-quasar correlation function, galaxy interactions are crucial to creating binary quasars (see KFM99, Mortlock & Webster 2000) and can be used as a tool to study the triggering of nuclear activity in galaxies (e.g. Osterbrock 1993).

Nonetheless, we still have puzzling examples of WSQPs whose members have startlingly similar optical spectroscopic properties but no evidence for a lens. One example is the optical quasar pair Q2345+007A,B (Tyson et al. 1986). With a separation of $7''.3$, Q2345+007 is the most prominent ‘dark matter’ gravitational lens candidate. Optical spectra of the two image components show exceptional intrinsic similarity in both line profile and velocity (e.g., $z = 2.15$, $\Delta v_{B-A} = 15 \pm 20 \text{ km s}^{-1}$; Steidel & Sargent 1991; hereafter SS91). Slight differences may be explainable as the combined effect of time variability in the source and time delays produced by the lens (Small et al. 1997). After nearly 20 years of study including deep optical and infrared imaging (Nieto et al. 1988, Weir & Djorgovski 1991, Bonnet et al. 1993, Gopal-Krishna et al. 1993, McLeod et al. 1994, Fischer et al. 1994, Pello et al. 1996) and VLA radio imaging (Patnaik et al. 1996), this pair remains the most obstinate mystery. Either massive, concentrated dark matter near the line of sight is acting as a gravitational lens, or two neighboring quasars have virtually identical spectral characteristics yet significantly different luminosities.

In this paper we present a deep X-ray image of Q2345+007 obtained with the Chandra X-ray Observatory (CXO). Using the superb sensitivity and resolution of the CXO we address two questions. First, we search the field for extended X-ray emission from hot baryons in the lens, which allows us to detect an optically dark halo. We cannot detect a baryon-free halo, since the X-ray emission depends on the hot baryons in the halo, but we can detect halos with reduced baryon fractions. Second, we test whether the X-ray flux ratios and spectra of the images are consistent with the lens hypothesis. We describe the CXO observations next in § 2, and supporting Kitt Peak optical imaging in § 3. We discuss the search for extended emission from a lensing cluster in § 4, and contrast the properties of the two quasars in § 5, summarizing in § 6.

2. CHANDRA OBSERVATIONS AND ANALYSIS

Q2345+007 was first observed by the CXO on May 26, 2000 for 25.2ksec using the back-illuminated S3 chip of

the Advanced CCD Imaging Spectrometer (ACIS) in faint, timed-event mode. We offset the pointing by $1'$ in spacecraft Y -coordinate from the Chandra aimpoint, to allow for imaging of any extended emission all within one ACIS node. It was observed again on June 27, 2000 in the same configuration, for 52.6ksec. However, because of an incorrectly configured bias-only run in the previous ACIS segment, event rates were about 20 times as high as expected from the chips (I1 and I3) processed by Front End Processors (FEP) 0 and 3. Due to the telemetry saturation, this created up to 50% downtime in these chips. Telemetry dropouts are fully accounted for in the final exposure times, but the aimpoint chip S3 was in any case not affected.

We have used data reprocessed (in April 2001) at CXC³. We then ran XPIPE (Kim et al. 2000) which was specifically designed for the Chandra Multi-wavelength Project (ChaMP; Green et al. 2000). Data screening applied in the CXC Level 2 processing excludes events with bad grades (mostly cosmic ray events) and events with status bits set such as bad pixels and columns. Additional bad pixels and columns were excluded by examining events in the chip coordinates in each chip. To remove time intervals of high background rates, we make a light curve and exclude those time intervals with $3\text{-}\sigma$ or greater fluctuation above the mean background count rate. Given different characteristics between BI and FI chips, this is done separately for each ACIS chip. The remaining exposure time for the back-illuminated S3 chip is 64,998 sec.

For source detection, we have applied the `wavdetect` algorithm (Freeman et al. 2002), available in the *Chandra Interactive Analysis of Observations* (CIAO) software package.⁴ `Wavdetect` is more reliable than the traditional `celldetect` algorithm for finding individual sources in crowded fields and for identifying extended sources, but the algorithm tends to detect spurious sources near the detector edge. To avoid such false detections, we generate an exposure map for each chip (assuming a monoenergetic distribution of source photons at 1.5keV) and apply an exposure threshold parameter to be 10%. After performing various tests to find the most efficient parameters (see Kim et al. 2000), we select a significance threshold parameter to be 10^{-6} , corresponding to 1 spurious source per CCD chip. We use scale parameters of 1, 2, 4, 8, 16, 32, and 64 pixels to cover a wide range of source scales, thus accommodating the PSF variation as a function of off-axis angle. For other parameters, we have used default values given in CIAO2.1.

As shown in Figure 1, Q2345+007 A and B are well-resolved and strongly detected in the image. The Chandra astrometry for the pair corresponds closely ($\sim 0.3''$) to the optical counterpart positions, as expected from Chandra’s absolute aspect quality (Aldcroft et al. 2000). We perform our own aperture photometry at the `wavdetect` positions of the 46 detected sources on this chip, which yields sources between 7 to 608 net counts (0.5-8 keV), and S/N from 1.6 to 24.

3. MOSAIC OPTICAL IMAGING OBSERVATIONS

³ CXCDs versions R4CU5UPD14.1, along with ACIS calibration data from the Chandra CALDB 2.0b.

⁴ CIAO may be downloaded from <http://asc.harvard.edu/ciao/>.

Several lensing cluster candidates have been suggested from analysis of deep optical images. As part of the Chandra Multiwavelength Project (ChaMP) for followup of Chandra serendipitous sources (Green et al. 2000), on UT 29 September, 2000 and 22 Aug 2001, we obtained images in Sloan g' , r' , and i' filters at the CTIO 4meter Blanco telescope using the wide-field MOSAIC camera, which has eight 2048×4096 chips in a 4×2 array comprising a $36 \times 36'$ field of view. We reduced the images using the MSCRED (v4.1) package (Valdes & Tody 1998; Valdes 1998) in the IRAF environment (Tody et al. 1986). This proceeds via the usual initial calibration, subtracting median-combined bias frames and dividing by similarly prepared dome flats. Additionally, we correct for electronic crosstalk between pairs of CCDs sharing readout electronics. We then make a single image in each filter by median-combining multiple object frames, effectively rejecting all of the celestial objects in the final frame. From this we create a fringe-correction frame in each filter with the large-scale variation removed, and interactively subtract scaled versions from every exposure in each given filter. We then generate the sky flat for large scale corrections, again via median filtering, this time of fringe-corrected object frames. This sky flat is divided into every object frame.

From our MOSAIC images, we determined the (previously unpublished) positions of optically-identified lens candidates discussed below, listed for convenience in Table 1. These optical positions are based on an astrometric solution of rms $\sim 0.1''$ obtained by matching detected objects to the GSC2.2 catalog.⁵ On each observing run, we obtained for this field 3 dithered images per filter. After we flag bad pixels and charge bleeds from severely saturated stars in each image, we project them onto the tangent-plane. Removal of remaining large-scale gradients and scale differences between dithered images allows for combination into a final single stacked image in each filter. These nights were probably photometric, since the scaling values were close to one.

We used the MOSAIC images to determine the optical flux ratios of the quasar pair in our 3 filters. These are tabulated as magnitude differences in Table 2, along with previously published values, for convenience. We discuss the evident variability in § 5.3.

4. THE SEARCH FOR THE LENS

We now search for X-rays from any extended halo centered on the WSQP, and also measure X-rays from published optical cluster candidates. In § 4.1 we describe our search for X-ray emission from any lensing halo, and in § 4.2 we compare the extended X-ray emission to the optically-identified cluster candidates inferred from the distribution of galaxies in the field (Bonnet et al. 1993; Pello et al. 1996). In § 4.3 we discuss the implications of our measurements for the lens hypothesis.

4.1. Search for Extended X-ray Emission

No significant extended emission sources are evident to the eye on the ACIS-S3 image. When searching for faint extended sources, however, it is important to minimize background contamination. The ACIS particle background increases significantly below 0.5keV and again at high energies. To optimize detection of a weak cluster signal, we first filtered the cleaned, combined image to include only photons between 0.5 and 2keV. We then masked out pixels within a radius encompassing 95% of the encircled energy around all point sources detected by `wavdetect`. This image is divided by the appropriate ACIS-S3 exposure map, which takes account instrumental features (effective area, quantum efficiency, telescope vignetting) as well as relative exposure due to the dither pattern. Further division by the exposure time yields a normalized image with pixel values in photons $\text{cm}^{-2} \text{s}^{-1}$. To facilitate the search for nearby extended sources, we smoothed the point-source-subtracted image using a $10''$ FWHM Gaussian. Figure 2 shows several marginal excesses at $\sim 20\%$ above the background level of $2 \times 10^{-10} \text{photons cm}^{-2} \text{sec}^{-1} ''^{-2}$ (corresponding to 0.16 counts/sec across the entire chip). Several low-level ($\sim 10\%$) features in the normalized image in Figure 2 partially coincide with features in the exposure map. This may be because the telescope effective area varies in the 0.5-2keV bandpass and the assumed spectrum used to compute the exposure map (monoenergetic 1.5keV) may not represent the incident spectra very well across the image. More detailed simulations for detecting extended structures in ACIS images are called for, but beyond the scope of this paper. None of the features were detected by our wavelet detection analysis, so we do not consider any of the apparent fluctuations to be significant unless they appear clearly in radial profiles.

In Table 1, we tabulate the X-ray positions (based on the peak flux in the smoothed image) of apparent extended excesses near Q2345+007. We summed the X-ray counts in $10''$ annuli centered on a point midway between the two QSO images, and extending to a $2'$ radius, and detect no excess over the background. To derive an upper limit on the extended source flux, we denote source counts S and background counts B (where B has been estimated from an area A_B but normalized to the source area A_S).⁶ The random 1σ deviation in counts is $\sigma = \sqrt{S + kB}$, where $k = (1 + \frac{A_S}{A_B})$. If we define a source count upper limit at N standard deviations, then our source count upper limit becomes

$$S = N\sigma = \frac{N}{2} \left(N + \sqrt{N^2 + 4kB} \right)$$

We estimate the background from an area $A_B \gg A_S$, and thereby derive a 95% upper limit of fewer than 44 counts from any cluster within a circle of $1'$ radius centered on the WSQP, corresponding to a count rate of $7 \times 10^{-4} \text{sec}^{-1}$. Considering a Raymond-Smith model with a reasonable range⁷ of parameters and Galactic absorption, the corresponding upper limit on the 0.5 – 2 keV flux is around

⁵ The Guide Star Catalogue-II is a joint project of the Space Telescope Science Institute and the Osservatorio Astronomico di Torino. Space Telescope Science Institute is operated by the Association of Universities for Research in Astronomy, for the National Aeronautics and Space Administration under contract NAS5-26555.

⁶ Source counts are derived from total counts T in area A_S via $S = T - B$.

⁷ The unabsorbed flux is derived, i.e., from outside the Galaxy. Changes in the assumed spectral models from 2 to 8keV result in changes of $\sim 15\%$ in the value of the derived flux.

$2 \times 10^{-15} \text{erg cm}^{-2} \text{s}^{-1}$. This illustrates Chandra’s excellent sensitivity to faint sources, even when extended.⁸

4.2. Observed Cluster Constraints

Our 0.5-2keV flux upper limit of $2 \times 10^{-15} \text{erg cm}^{-2} \text{s}^{-1}$ within $1'$ of the WSQP clearly yields a stringent limit on the existence of any lensing cluster. Assuming a $T = 2 - 3$ keV spectrum, this upper limit corresponds at $z \sim 1$ to a $0.5 - 2$ keV (rest frame) luminosity of $1.2 \times 10^{43} \text{erg s}^{-1}$ (1.6×10^{43} for $\Omega = 0.3$). An $r = 1'$ aperture at $z = 1$ corresponds to 0.5Mpc (0.6Mpc for $\Omega = 0.3$) and encloses about a half of the total luminosity for a typical cluster with the surface brightness described by a β -model with a core radius of 0.25 Mpc and $\beta = 0.6$ (Jones & Forman 1984). With this correction, our upper limit corresponds to a typical luminosity of a galaxy group with $T \sim 2 - 3$ keV (e.g., Hwang et al. 1999 and references therein), so our estimate is self-consistent. All luminosities, sizes and distances are calculated assuming $H_0 = 50 \text{ km s}^{-1} \text{ Mpc}^{-1}$, $\Omega_0 = 1.0$, and $\Lambda = 0.0$ unless otherwise noted (we also give $\Omega_0 = 0.3$ values). This represents by far the strongest constraint on the X-ray luminosity of any dark lens candidate to date (cf., Chartas et al. 2001).

It is certainly possible that a massive cluster that is *not* centered on the WSQP could also produce the observed image splitting. Therefore, we also investigate apparent flux excesses in the vicinity ($< 1.5'$) of the quasar pair. However, the required mass of the lensing cluster would rise with angular distance from the WSQP, so that our flux limits constrain the existence of such a cluster even more strongly at larger angles.

The closest significant excess of extended X-ray emission to the WSQP is CXOJ234817.6+005717. Centered about $27''$ from the center of the WSQP, it has a peak flux of about $0.0544 \text{ counts cm}^{-2} \text{s}^{-1} \text{arcsec}^{-2}$. The radial profile of this excess, determined with possible nearby extended sources removed, is shown in Figure 3. The excess contributes just 11 ± 5 counts above background. At just 2.2σ , we find this source to be of questionable certitude. A more credible 2σ upper limit to the flux yields $9 \times 10^{-16} \text{erg cm}^{-2} \text{s}^{-1}$ from 0.5-2keV.

Bonnet et al. (1993) identified a cluster center they label **C1** from a weak gravitational shear field pattern suggesting a lens velocity dispersion $\sigma_v \sim 1200 \text{ km s}^{-1}$. The peak X-ray flux of the above extended source corresponds to a position just $8''$ from C1. Pello et al. (1996) claimed an excess of galaxies with photometric redshifts $z \sim 0.75$, which is $13''$ from C1 and $21''$ from CXOJ234817.6+005717. However, centroids may naturally have somewhat different positions because optical galaxies may not follow the overall mass distribution, and the cluster also may not be virialized. Assuming that all 3 objects (C1, the Pello et al. $z=0.75$ optical galaxy excess, and CXOJ234817.6+005717) can be identified as the same object, the $0.5 - 2$ keV luminosity upper limit is $2.8 \times 10^{42} \text{erg s}^{-1}$ ($3.6 \times 10^{42} \text{erg s}^{-1}$ for $\Omega = 0.3$) more similar to an isolated elliptical galaxy or a small group than to a rich $\sigma_v \sim 1200 \text{ km s}^{-1}$ cluster, suggesting that the large velocity dispersion estimate is the result of a line of sight projection. In any case, at

a transverse distance of $\sim 220h_{50} \text{kpc}$, such a mass is too small to produce the observed pair separation by lensing.

Bonnet et al. also identified the galaxy G2⁹ as having a position consistent with C1 within the errors ($\sim 9''$ from the best centroid of C1). At $15''$ from G2, CXOJ234817.6+005717 is clearly not consistent with emission from that galaxy. Another apparent X-ray excess CXOJ234816.9+005811 is an arcminute from the WSQP centroid, but $7''$ from the galaxy G1 identified by Bonnet et al. (1993). However, our radial profile centered either on CXOJ234816.9+005811 or on the position of G1 reveals no significant excess above background, even when the other nearby extended sources are excised.

4.3. Comparison to Required Lens

We start by assuming the WSQP is a lens produced by a simple, singular isothermal sphere (SIS, see Schneider, Ehlers & Falco 1992). The image separation $\Delta\theta = 8\pi(\sigma_v/c)^2 D_{LS}/D_{OS}$ depends only on the velocity dispersion of the potential σ_v and the ratio of the comoving distances between the lens and the source, D_{LS} , and the observer and the source, D_{OS} . Since we failed to detect a lens cluster, we will get the most conservative limits if we assume the lens lies at the “minimum flux redshift,” the redshift that would minimize the observed X-ray flux. If we neglect K-corrections, the flux from the lens is

$$F = \frac{L}{4\pi D_{OL}^2 (1+z_l)^2} \propto \left[\frac{D_{OS} r_H}{D_{OL} D_{LS} (1+z_l)} \right]^2 \quad (1)$$

where r_H is the Hubble radius c/H_0 . This flux diverges at low redshift because of the proximity of the cluster and at high redshift because of the mass of the cluster. For $\Omega_0 = 1$ the flux is minimized at $z_l = 0.92$, which we will round to $z_l = 1$ for simplicity.

Now using a SIS model for the lensing mass, the large image separation of $7''.3$ implies a cluster velocity dispersion of $\sigma_v = 860 \text{ km s}^{-1}$ or a cluster mass of $1.3 \times 10^{14} M_\odot$. We emphasize that this is the *minimum* enclosed mass or dispersion required at this redshift to induce the observed pair separation. Combining the $L_X - \sigma_v$ relation from, e.g., Mulchaey & Zabludoff (1998) and the $L_X - T$ relation from, e.g., Markevitch (1998), and neglecting any possible cosmological evolution of these relations for a qualitative estimate, we obtain $L_X(0.5 - 2 \text{ keV}) \approx 2 \times 10^{44} \text{erg s}^{-1}$ and $T \approx 5 \text{ keV}$ for such a cluster. At $z = 1$, this corresponds to $f_X(0.5 - 2 \text{ keV}) \approx 4 \times 10^{-14} \text{erg cm}^{-2} \text{s}^{-1}$ (3×10^{-14} for $\Omega = 0.3$). Again assuming a typical cluster brightness distribution and dividing by 2 to convert to the $r = 1'$ aperture, we can see that *our 95% flux limit is an order of magnitude below this minimum required flux estimate*. If the lens were a dark cluster lacking not only galaxies but also gas, the gas fraction would have to be ~ 3 times lower than that in known clusters. At low redshift, all well-studied clusters (at least in the relevant range of radii and masses) have similar values of the gas fraction (e.g., Mohr, Mathiesen, & Evrard 1999; Vikhlinin, Forman, & Jones 1999) so such a deviation appears to be extremely unlikely. We conclude that a single cluster acting as a lens is not a plausible scenario for Q2345+007.

⁸ If there is any residual flux from the WSQP scattered beyond the radius containing 95% of the total energy, our estimated cluster flux upper limit is conservative.

⁹ G1 is the brighter galaxy. Labels in Bonnet et al. (1993) for G1 and G2 are incorrectly swapped in all but their Figure 2.

In other lenses clearly due to a combination of a cluster and a galaxy (particularly Q0957+561; Keeton et al. 2000), a massive, luminous lens galaxy dominates the image splitting. Here we see no such candidate galaxy, even in the infrared, to a limit of approximately $L_*/10$ near redshift unity. Such a galaxy, unless completely different from all other known lens galaxies (e.g., Kochanek et al. 2000, Xanthopoulos et al. 1998), must make a negligible contribution to the overall image separation and modifies our estimate of the critical radius of the putative dark halo only by a factor of $1 - 2b_{gal}/\Delta\theta$ with $b_{gal} \ll 1''$.

5. ARE THEY IMAGES OF THE SAME QUASAR?

We have failed to find a lens. While a dark matter lens is not ruled out, the pair could also be shown to be a binary quasar by evidence that the components' spectral energy distributions are different. We explore this by first determining the X-ray properties of the two quasars in § 5.1, followed by a discussion of the possible effects of absorption and extinction on the flux ratios in § 5.2. In § 5.3 we compare the flux ratios from the near infrared to the X-ray bands to conclude that they are probably different quasars. We discuss the remaining puzzle of the strikingly similar optical/UV spectra of the components in § 5.4.

5.1. The X-ray Properties of the Quasars

The total broad band (0.3-8keV) counts from the QSOs are 358.5 ± 20 and 54.8 ± 8 for components A and B, respectively. The broad band X-ray flux ratio is 6.55 ± 0.50 .

As a first check of whether the QSOs have similar X-ray spectra, we measure their hardness ratio, $HR = (H - S)/(H + S)$, using the hard counts (H) from 2.5 - 8.0keV and the soft counts (S) from 0.3 - 2.5keV. While differences in instrument and telescope calibration are completely negligible at these spacings, the benefit of comparing hardness ratios directly are that no spectral models need be fitted to the data. We find $HR_A = -0.89 \pm 0.02$ and $HR_B = -0.55 \pm 0.11$, which are significantly different (at 3σ).

However, although optical magnitudes suggest little differential reddening (see § 5.2 below), absorption along different sightlines to the QSO might still produce a significant difference in HR if the absorbers are not dusty. We also calculate the X-ray flux ratio in a bandpass that is much less subject to absorption. In the 1.6-8 keV band (5-25 keV in the QSO restframe) the X-ray flux ratio is smaller, 2.3 ± 0.5 . This large difference from the broad-band flux ratio is expected given their differing hardness ratios.

A test for differential absorption requires X-ray spectral modeling. For spectral analyses, we used the latest (CALDB2.7) ACIS-S3 FITS Embedded Function (FEF) files and corresponding gain tables. The new FEFs are analytic fits based on a physical model of the back-illuminated CCD, developed by the MIT ACIS/IPI team, and adjusted to the on-orbit gain of the S3 chip as determined by the flight calibration sources. These FEFs are used to generate a Response Matrix File (RMF), which maps the incident photon energy to ACIS pulse height (deposited charge). An Ancillary Response File (ARF) calibrates the effective collecting area of a specified source region on ACIS as a function of incident photon energy.

We extract ACIS PI spectra from a $3.5''$ region around each QSO, using the `psextract` script described in the standard thread for CIAO2.1. This script creates an aspect histogram file, and the RMF and ARF calibration files appropriate to the source position on chip (which is time-dependent due to dither) and CCD temperature (-120 C).

We first group the Chandra spectra into bins containing at least 10 counts each. We test four spectral models to test permutations that link or decouple the power-law and absorbing columns of Q2345+007A and B. Results for all four models are compiled in Table 3. Model (1) fixes ($z = 0$) absorption at the Galactic value, but allows the power-law slope and flux normalization to vary for each QSO, as

$$N(E) = A_i E^{-\Gamma_i} e^{-N_H^{Gal} \sigma(E)} \text{ photons cm}^{-2} \text{ s}^{-1} \text{ keV}^{-1}$$

In this formula, A_i is the normalization and Γ_i the *global* power-law photon index for the individual QSOs. N_H is the equivalent Galactic neutral hydrogen column density $3.81 \times 10^{20} \text{ cm}^{-2}$ which characterizes the effective absorption (by cold gas at solar abundance), with $\sigma(E)$ the corresponding absorption cross-section (Morrison & McCammon 1983). For determining the best-fit parameter values, we use Powell optimization with Primini statistics (Kearns et al. 1995). This fit yields a typical continuum slope $\Gamma_A = 2.19 \pm 0.15$ for the brighter component ($\chi^2_\nu = 1.1$). The fainter QSO shows a best-fit of $\Gamma_B = 0.79 \pm 0.4$ ($\chi^2_\nu = 0.6$). These confirm our impression from the hardness ratio that the observed energy distributions are not consistent.

There are not sufficient counts from B to independently fit both its absorbing column and power-law slope. However, a somewhat stronger test than Model (1) is available by assuming that A and B have identical total absorbing columns, fitting that column simultaneously (Model 2). The result is a column $N_H = 5.3 \pm 3.1 \times 10^{20} \text{ cm}^{-2}$, which yields slopes $\Gamma_A = 2.30^{+0.36}_{-0.30}$ and $\Gamma_B = 0.83^{+0.49}_{-0.44}$. Therefore, *if* the X-ray emission from A and B suffer identical absorption along the line of sight, we can confidently say that their intrinsic spectral energy distributions are inconsistent. Contour plots for this simultaneous power-law fit are shown in Figure 5. Not surprisingly (since A dominates the total counts) we find similar results when using for B the best-fit column from A alone.

Rather than accepting the power-law difference as intrinsic, we might entertain the possibility that B suffers from strong absorption, since this can mimic a flat power-law slope in low S/N X-ray spectra. If we assume that the system is lensed, then the underlying X-ray power-law continuum slopes should be indistinguishable, even though their line-of-sight absorption may vary. We thus fit Model (3) by assuming a single power-law slope, but allowing for different absorbing columns between the two components. The best-fit continuum slope is $\Gamma = 2.14^{+0.34}_{-0.28}$, and the absorbing columns are quite different: $N_{H,A} = 3.4^{+3.5}_{-2.9} \times 10^{20} \text{ cm}^{-2}$ and $N_{H,B} = 43.9^{+29}_{-18} \times 10^{20} \text{ cm}^{-2}$. Contour plots for this simultaneous absorption column fit are shown in Figure 5.

If we also allow the absorption columns to differ between A and B (Model 4), the difference between the best-fit power-law slopes becomes insignificant. This is because, as expected, the small number of counts in B are insufficient to constrain both parameters. While the parameters for A

change little, for B, we find $N_{H,B} = 23.6_{-19.2}^{+28.1} \times 10^{20} \text{ cm}^{-2}$ (consistent with no absorption) and $\Gamma_B = 1.37_{-0.66}^{+0.79}$.

The observed range of continuum slopes in radio-quiet quasars is $1.5 < \Gamma_{2-10\text{keV}} < 3$ with a mean of $\bar{\Gamma} = 2.0 \pm 0.25$ (1σ dispersion; George et al. 2000). Therefore, the very flat slope measured here for B might be unrealistic, possibly affected by line-of-sight absorption. Higher S/N X-ray spectroscopy would reveal whether it is the absorption, the intrinsic continua, or both that differ between the two images. Only repeated observations, a daunting investment, can definitively reveal whether the observed differences are due to variations in a single lensed QSO whose images suffer differing time delays. Since the evidence for absorption is weak, if Q2345+007A,B are indeed lensed, this would predict that a program to monitor a suitable sample of single luminous QSOs over a period of a few years would result in the discovery of large temporal variations in the X-ray continuum slopes of individual objects.¹⁰ Sufficiently large changes in either the column or continuum slope in single QSOs have not been observed to date (e.g., Lawson & Turner 1997).

5.2. Intrinsic or Intervening Absorbers

Could a lens + absorption interpretation explain other data? From our MOSAIC imaging, or from the colors published by Pello et al. (1996), the difference between $g' - r'$ and $r' - i'$ for the two images is negligible (-0.032 ± 0.02 and 0.037 ± 0.02 , respectively). The optical colors show little evidence for reddening relative to the main stellar locus, and indeed are quite blue in $g' - r'$, as expected for QSOs at this redshift (Richards et al. 2001). Thus any putative absorber is likely to be warm (ionized). Warm X-ray absorbers are usually accompanied by a significant decrease in relative X-ray strength, as might be in evidence in the larger $\alpha_{\text{ox}} = 1.7$ of Q2345+007B, but also by evident absorption in the rest-frame ultraviolet spectrum, particularly in the blue wing of CIV (Brandt, Laor & Wills 2000).

High S/N restframe UV spectra of Q2345+007 A and B (SS91) show little difference between the CIV profiles, and no strong intrinsic absorption. Indeed, absorption lines of intervening CIV systems at $z_{\text{abs}} = 1.798, 1.799$ and 1.983 are all stronger in A than in B. Near the CIII] emission line, B shows stronger absorption lines in the blue wing, while A shows an overall lower profile. However, this absorption is most likely due to intervening (not intrinsic) absorption at $z = 1.7717$ (SS91). Intervening absorbers such as these in galactic halos or disks have UV columns and ionization levels that are far too small to cause detectable absorption of the X-ray emission (O’Flaherty & Jacobsen 1997). Interestingly, an intervening CIV absorber at $z \sim 0.75$ (same as the putative cluster C1) would not show strong lines within the wavelength range of the existing spectra. SS91 find evidence for a weak ($W_\lambda \sim 1$) MgII absorption doublet in Q2345+007B at this redshift. The problem is that an ionized absorber at $z = 0.75$ would be optically bright ($R < 22.5$; Cohen et al. 2000), and easily detected in the deep optical imaging.

The limits on a galaxy that might cause such intervening absorption are quite stringent ($B \geq 25$ and $H > 22.5$; Fis-

cher et al. 1994; Munoz et al. 1998). Mg II absorbers are usually associated with galaxies of Hubble types E through Sb (Steidel 1993). Even a normal L^* Sc galaxy would be 2 mag brighter than the H magnitude limit at this redshift. An early-type L^* galaxy would be at least 4 mag brighter (see the closely related discussion for Q1634+267A,B in Peng et al. 1999). So no reasonable candidates exist for a line-of-sight absorber to account for the X-ray properties of Q2345+007B.

5.3. Optical/X-ray Flux Ratios of the WSQP

For comparison to the optical and infrared bands, the epoch 1990 flux ratios in B, R, I, J and K bands from Pello et al. (1996) are 3.1, 3.0, 2.9, 4.2, and 4.0 respectively. The difference between these flux ratios and those in the X-ray band (6.55, corresponding to 2.0 on a magnitude scale) seems significant enough to rule out the lens interpretation.

Weir & Djorgovski (1991) found evidence for variation in the magnitude difference between the two components, and Gopal-Krishna et al. (1993) argued that detection of a time delay is crucial to proving that the WSQP is indeed a lens. If the pair is lensed, then the expected time delay is about a year. A comparison with optical flux ratios more nearly contemporaneous to the X-ray observation is desired. The dates of our own optical imaging do not match the Chandra observations, but begin less than 2 months after. We compile in Table 2 the magnitude differences between Q2345+007 A and B in several optical filters. Flux ratios extracted from our (epoch 2000.75) MOSAIC image using SExtractor (Bertin & Arnouts 1996) in Sloan $g', r',$ and i' filters are 5.6, 5.5, and 5.3, respectively. With errors at most ~ 0.1 for each ratio, these all agree with each other and suggest no strong differential reddening of a lensed pair. However, these optical ratios still differ from the broadband X-ray flux ratio at the $\sim 2\sigma$ level. Our epoch 2001.63 images show ratios of 4.5, 4.6, 4.4, which differ at $> 3\sigma$ from the X-ray flux ratio.¹¹ The X-ray (0.3-8keV) flux ratios we measure during the separate Chandra observations of May and June 2000 are 8.2 ± 2.1 and 6.2 ± 1.0 , respectively. Given the evidence of variability, we can not rule out the possibility that at the epoch of the X-ray observations, the optical ratios were identical to the X-ray flux ratio.

KFM99 developed a statistical proof for comparing the optical and radio properties of the WSQP population to demonstrate that most WSQPs must be binary quasars rather than lenses, and that their incidence was explained by the triggering of quasar activity during galaxy mergers. KFM99 classified the quasar pairs as both radio-faint (denoted O^2), both radio-bright (O^2R^2), or radio-mixed (O^2R). The radio-mixed pairs have wildly discrepant optical/radio flux ratios (by factors of 50 or more) and are clearly *binary* quasars rather than lenses. The ratio of radio/optical power spans 10^4 in optically-selected quasars, and the radio-loud fraction is $P_R \sim 10\%$ (e.g., Hooper et al. 1995). Hence the existence of each O^2R pair implies the existence $1/2P_R \sim 5 O^2$ pairs, and KFM99 could show statistically that at most 8% (22%) of the WSQP pairs

¹⁰ Analogous predictions for optical spectroscopic variability by SS91 were later confirmed by Small et al. (1997).

¹¹ The mean change in magnitude difference for stars we find in the same filter at the 2 different epochs is $0 \pm 0.12\text{mag}$.

could be gravitational lenses at a $1\text{-}\sigma$ ($2\text{-}\sigma$) limit. These limits still admit a population of optically dark clusters equal to the normal cluster population, so the possibility of optically dark clusters still remains.

By imaging an O^2 quasar pair with Chandra we can see if the X-ray and optical flux ratios are discrepant – an “ O^2X ” pair is not a lens. The only disadvantage of using quasar X-ray emission is that it is more common than radio emission, and is even considered *the* signature of an active nucleus. Nonetheless, X-ray to optical flux ratios span a range of ~ 400 (Pickering, Impey & Foltz 1994), so it is probable that binary quasars will show discrepancies in their α_{ox} values.

Assuming a power-law continuum slope of $\Gamma = 2.4$ from spectral fitting of A and the Milky Way gas column, the observed count rate corresponds¹² to an (absorbed) X-ray flux in this band for QSO A of $F_{X,A} = 2.52 \times 10^{-14} \text{erg cm}^{-2} \text{s}^{-1}$, while for B the flux is 0.386 in the same units. From the unabsorbed values (20% larger for this slope and N_H), the inferred monochromatic rest-frame luminosities at 2 keV are $\log L_{2\text{keV}} = 26.84$ and 26.02 (in $\text{erg s}^{-1} \text{Hz}^{-1}$), or 45.11 and 44.30 broadband in erg s^{-1} .

Using the optical B magnitudes from Pello et al. (1996), the logarithm of the monochromatic 2500Å optical luminosities (in units erg s^{-1}) are 31 and 30.5, for A and B respectively. These correspond to $M_B^A = -26.08$ and $M_B^B = -24.84$ in absolute magnitudes at 4400Å (Schmidt & Green 1983). We assume an optical spectral index of $\alpha = -0.5$, consistent with that found in SDSS QSOs (with a spread of 0.65; Richards et al. 2001), with specific optical normalization from Marshall et al. (1984). The resulting α_{ox} values¹³ are 1.60 and 1.72. The value for A is quite normal for optically-selected QSOs (e.g., Green et al. 1995, Yuan et al. 1998), while the value of 1.72 for B is more similar to the values found for absorbed QSOs (Green et al. 2001; Brandt, Laor & Wills 2000). If there is strong absorption along the sightline to QSO B, it is not detectable in an X-ray spectrum containing only 55 counts, but more importantly not evident in its optical colors or restframe UV spectroscopy, as discussed above.

5.4. Optical Spectra

The exceptionally detailed intrinsic similarity in the optical spectra of the quasar images (SS91) remains the obstinate core of a long-running mystery. The differences seen are primarily in intervening absorbers, and in the pairs’ CIII] emission line strength. The intervening absorbers are expected to differ in either the lens or binary scenario, but more so in the latter. But accounting for differences in the *emission line* profiles is more problematic. Microlensing by stars in the lens could account for $\sim 10\%$ differences at most (Schneider & Wambsganss 1990).¹⁴ However, in a lens scenario, the differences are most likely due to intrinsic profile variations in a single quasar that occur on a characteristic timescale less than the time delay between the two images, roughly about a year (9 months for $z_{\text{lens}} = 1.5$;

~ 1.8 years for $z_{\text{lens}} = 0.75$). Small et al (1997) confirmed that the observed differences between emission lines in the Q2345+007 images are consistent with the spectral differences seen on 1-1.5 year timescales in *individual* QSOs. So the few observed spectral differences do not rule out the lens interpretation.

Given that the current study refutes the lens hypothesis, is it likely for two *distinct* QSOs to have spectra that are as similar as observed? Quasar broad emission line strengths and profiles seem to be loosely correlated with other QSO properties, like luminosity, α_{ox} , and narrow emission line strength (e.g., Baldwin 1977; Laor et al. 1997; Green et al. 2001). The great similarity in emission lines in Q2345+007 A and B argues that, if they are distinct objects, their luminosity, the geometry of their emission regions *and* their inclination angle should all be similar. Detailed empirical tests on the probability of achieving such similar spectra at random among a sample of unrelated quasars require large databases of quasar spectra, uniformly analyzed, and with similar S/N and resolution. Such studies are beyond the scope of this paper, but adequate measurement datasets are now becoming available (Forster et al. 2000).

6. SUMMARY

We conclude that Q2345+007A,B is a quasar binary.

First, we find *no* evidence for a halo in the field sufficiently massive to produce the image separation, provided that halo contains at least 1/3 of the normal cluster baryon fraction. Mechanisms may exist to suppress star formation in galaxies (e.g. Elmegreen & Parravano 1994) or to produce only exceptionally low surface brightness galaxies (e.g. Sprayberry et al. 1995) thereby diminishing the optical luminosity of cluster members. There is no such mechanism known that could significantly reduce the baryon fraction in a cluster potential well. The energy injection from star formation or AGN would need to be adequate not only to heat and eject gas from the galaxies, but also from the massive cluster potential. Even if the energetics were plausible, we are unable to find any of the concomitant optical or infrared emission (e.g. McLeod, Rieke, & Weedman 1994).

Second, the two quasars have X-ray properties inconsistent with the lens hypothesis. The X-ray flux ratios are inconsistent with the optical flux ratios. Their X-ray spectral properties also differ significantly, and we find no evidence for either extinction or absorption that might explain the inconsistency in terms of the lens hypothesis.

Significantly deeper spatially resolved X-ray spectroscopy could show more definitively that the pair is a binary. The best available hope to prove the pair is lensed would be detection of a time-delay in correlated variability. Optical or near-IR detection of host galaxies in the QSO images could also provide strong arguments for or against the lens hypothesis.

The X-ray evidence in the field of Q2345+007 does not support the lens hypothesis. This WSQP is thus likely

¹² We use the Chandra Portable, Interactive Multi-Mission Simulator (PIMMS; originally Mukai 1993).

¹³ α_{ox} is the slope of a hypothetical power-law from 2500 Å to 2 keV; $\alpha_{\text{ox}} = 0.384 \log(\frac{L_{2500}}{L_{2\text{keV}}})$. Use of the nominal best-fit slope of $\Gamma_B = 0.9$ for B does not significantly affect the α_{ox} values ($< 1\%$ change).

¹⁴ The modeling of microlensing effects to date has assumed Keplerian cloud orbits in the BLR, which yield greater predicted differences than infall models. More recent outflow disk wind models (Murray & Chiang 1997; deKool & Begelman 1995; Elvis 2000) are highly aspect dependent and may yield larger differences in microlensing models.

to be a binary quasar, and currently stands as the example with the highest redshift, the largest separation, and the most detailed agreement between optical/UV spectra of its components. We may be studying a pair of luminous QSOs whose hosts, separated by $\sim 60h_{50}\text{kpc}$, have a history of dynamical interaction. Plausible models hold that quasar activity is triggered by tidal interactions in a galactic merger, but that activation of the galactic nuclei occurs late in the interaction, when the nuclei are within $80 \pm 30\text{kpc}$ of each other (Mortlock et al. 1999). Simple dynamical friction models reproduce the observed distribution of projected separations of pairs, but predict that binary quasars are only observable as such in the early stages of galactic collisions, after which the supermassive black holes would orbit within the merger remnant. We speculate that Q2345+007 may represent the highest redshift example known of interaction-triggered but as-yet unmerged luminous AGN.

We thank Frank Valdes, Lindsey Davis, and the IRAF team for writing and helping with the MSCRED package. Thanks also to Brian MacLean at STScI for early help with the GSC2.2 catalog. Thanks to Ani Thakar at Johns Hopkins for help retrieving SDSS data. Funding for the creation and distribution of the SDSS Archive has been provided by the Alfred P. Sloan Foundation, the Participating Institutions, the National Aeronautics and Space Administration, the National Science Foundation, the U.S. Department of Energy, the Japanese Monbukagakusho, and the Max Planck Society. The SDSS Web site is <http://www.sdss.org/>.

This work was supported by CXO grant GO 0-1161X and NASA grant NAS8-39073. AD, PJG, DK, MM, and AS acknowledge support through NASA Contract NASA contract NAS8-39073 (CXC). CSK is supported by NASA grants NAG5-8831 and NAG5-9265.

REFERENCES

- Aldcroft, T. L., Karovska, M., Cresitello-Dittmar, M. L., Cameron, R. A., & Markevitch, M. L. 2000 *Proceedings of SPIE: X-Ray Optics, Instruments, and Missions III*, Vol. 4012 (2000), J. Truemper and B. Aschenbach, eds.
- Baldwin, J.A. 1977, *ApJ*, 214, 679 Ages: When Galaxies Were Young, ed. S. S. Holt & E. P. Smith (New York: AIP), 191
- Bertin, E. & Arnouts, S. 1996 *A&AS* 117, 393
- Bonnet, H., Fort, B., Kneib, J.-P., Mellier, Y., & Soucail, G. 1993, *A&A*, 280, L7
- Brandt, W. N. & Gallagher, S. C. 2000, *NewAR*, 44, 461
- Chartas, G., Bautz, M., Garmire, G., Jones, C., & Schneider, D. P. 2001, *ApJ*, 550, 163
- Cohen, J. G. et al. 2000, *ApJ*, 538, 29
- de Kool, M. & Begelman, M. C. 1995, *ApJ*, 455, 448
- Ebeling, H., Edge, A. C., Allen, S. W., Crawford, C. S., Fabian, A. C., Huchra, J. P. 2000, *MNRAS*, 318, 333
- Elmegreen, B. G. & Parravano, A. 1994, *ApJ*, 435, 121
- Elvis, M. 2000, *ApJ*, 545, 63
- Erben, T., van Waerbeke, L., Mellier, Y., Schneider, P., Cuillandre, J.-C., Costantini, F.J., & Dantel-Fort, M., 2000, *A&A*, 355, 23
- Faber, S. M. & Jackson, R. E. 1976, *ApJ*, 204, 668
- Fischer, P., Tyson, J. A., Bernstein, G. M., Guhathakurta, P. 1994, *ApJ*, 431, L71
- Forster, K., Green, P. J., Aldcroft, T. L., Vestergaard, M., Foltz, C. B., & Hewett, P. C. 2001, *ApJS*, 134, 35
- Freeman, P. E., Kashyap, V., Rosner, R., & Lamb, D. Q. 2002, *ApJS*, 138, in press
- George, I. M., Turner, T. J., Yaqoob, T., Netzer, H., Laor, A., Mushotzky, R. F., Nandra, K., Takahashi, T. 2000, *ApJ*, 531, 52
- Gopal-Krishna, Yates, M., Wiita, Paul J., Smette, A., Pati, A., & Altieri, B. 1993, *A&A*, 280, 360
- Green, P. J. et al. 1995, *ApJ*, 450, 51
- Green, P. J., Forster, K., & Kuraszewicz, J. 2001, *ApJ*, 556, 727
- Green, P. J. et al. 2000, *BAAS*, 31, 1493
- Holder, Gilbert P., Mohr, Joseph J., Carlstrom, John E., Evrard, August E., Leitch, Erik M. 2000, *ApJ*, 544, 629
- Hooper, E. J., Impey, C. D., Foltz, C. B., Hewett, P. C. 1995, *ApJ*, 445, 62
- Hwang, U., Mushotzky, R. F., Burns, J. O., Fukazawa, Y., & White, R. A. 1999, *ApJ*, 516, 604
- Xanthopoulos, E., Browne, I. W. A., King, L. J., Koopmans, L. V. E., Jackson, N. J., Marlow, D. R., Patnaik, A. R., Porcas, R. W., & Wilkinson, P. N. 1998, *MNRAS*, 300, 649
- Jones, C. & Forman, W. 1984, *ApJ*, 276, 38
- Kearns, K., Primini, F., & Alexander, D. 1995, *ADASS IV*, 331
- Keeton, C. R., Falco, E. E., Impey, C. D., Kochanek, C. S., Lehr, J., McLeod, B. A., Rix, H.-W., Munoz, J. A., & Peng, C. Y. 2000, *ApJ*, 542, 74
- Kim, D.-W. et al. 2000, *HEAD AAS*, 32, 2604
- Kochanek, C. S., Falco, E., & Munoz, J. A. 1999, *ApJ*, 510, 590 (KFM99)
- Kochanek, C. S., Falco, E. E., Impey, C. D., Lehar, J., McLeod, B. A., Rix, H.-W., Keeton, C. R. & Munoz, J. A. 2000, *ApJ*, 543, 131 Peng, C. Y.
- Laor, A., Fiore, F., Elvis, M., Wilkes, B. J., & McDowell, J. C. 1997, *ApJ*, 477, 93
- Lawson, A. J. & Turner, M. J. L. 1997, *MNRAS*, 288, 920
- Markevitch, M. 1998, *ApJ*, 504, 27
- Marshall, H. L., Avni, Y., Braccisi, A., Huchra, J. P., Tananbaum, H., Zamorani, G., & Zitelli, V. 1984, *ApJ*, 283, 50
- McLeod, B., Rieke, & M., Weedman, D. 1994, *ApJ*, 43, 528
- Mohr, J. J., Mathiesen, B., & Evrard, A. E. 1999, *ApJ*, 517, 627
- Morrison, R. & McCammon, D. 1983, *ApJ*, 270, 119
- Mortlock, D. J. & Webster, R. L., 2000, *MNRAS*, 319, 872
- Mortlock, D. J., Webster, R. L., & Francis, P. J. 1999, *MNRAS*, 309, 836
- Mukai, K. 1993, *Legacy* 3, 21
- Mulchaey, J. S. & Zabludoff, A. I. 1998, *ApJ*, 496, 73
- Munoz, J. A., Falco, E., Kochanek, C. S., Lehar, J., McLeod, B. A., Impey, C. D., Rix, H.-W., & Peng, C. Y. 1998, *Ap&SS*, 263, 31
- Murray, N. & Chiang, J. 1997, *ApJ*, 454, L105
- Nieto, J.-L., Roques, S., Llebaria, A., Vandierriest, C., Lelievre, G., Alighieri, S., Macchetto, F.D., & Perryman, M.A.C., 1988, *ApJ*, 325, 644
- O'Flaherty, K. S. & Jakobsen, P. 1997, *ApJ*, 479, 673
- Osterbrock, D. E. 199, *ApJ*, 404, 551
- Patnaik, A. R., Schneider, P., & Narayan, R. 1996, *MNRAS*, 281, 17P
- Pello, R., Miralles, J.M., Le Borgne, J.-F., Picat, J.-P., Soucail, G., & Bruzual, G., 1996, *A&A*, 314, 73
- Peng, C. Y. et al. 1999, *ApJ*, 524, 572
- Pickering, T. E., Impey, C. D., Foltz, C. B. 1994 *AJ*, 108, 1542
- Postman, Marc, Lubin, Lori M., Gunn, James E., Oke, J. B., Hoessel, John G., Schneider, Donald P., Christensen, Jennifer A. 1996, *AJ*, 111, 615
- Richards, G. T. et al. 2001, *AJ*, 121, 2308
- Rusin, D. et al. 2001, *AJ*, 122, 591
- Schmidt, M., & Green, R.F. 1983, *ApJ*, 269, 325
- Schneider, P., Ehlers, J., & Falco, E. E. 1992, *Gravitational Lenses*, XIV, (Berlin: Springer-Verlag)
- Schneider, P. & Wambsganss, J. 1990, *A&A*, 237, 42
- Small, T. A., Sargent, W. L. W., & Steidel, C. C. 1997, 114, 2254
- Sol, H., Vandierriest, C., Schneider, J., Lelievre, G., & Pedersen, H. 1984, *A&A*, 132, 105
- Sprayberry, D., Bernstein, G. M., Impey, C. D. & Bothun, G. D. 1995 *ApJ*, 438, 72
- Steidel, C. C. & Sargent, W. L. W. 1991, *AJ*, 102, 1610 (SS91)
- Steidel, C. C. 1993, in *Proc. 3d Teton Astronomy Conf., The Environment and Evolution of Galaxies*, ed. J. M. Shull & H. A. Thronson (Dordrecht: Kluwer), 263
- Tody D., et al., 1986, *IRAF Users' Manual*, National Optical Astronomical Observatories
- Tyson, J. A., Seitzer, P., Weymann, R. J., & Foltz, C. 1986, *AJ*, 91, 1274
- Umetsu, K. & Futamase, T. 2000, *ApJ*, 539, L5
- Valdes, F. 1998, in *ASP Conf. Ser. 145, Astronomical Data Analysis Software and Systems VII*, ed. R. Albrecht, R. N. Hook, & R. A. Bushouse (San Francisco: ASP), 53
- Valdes, F. & Tody, G. 1998, *Proc. SPIE*, 3355, 497
- Vikhlinin, A., Forman, W., & Jones, C. 1999, *ApJ*, 525, 47
- Weir, N. & Djorgovski, S. 1991, *AJ*, 101, 66
- Wittman, D., Tyson, J. A., Margoniner, V. E., Cohen, J. G., Dell'Antonio, I. P. 2001, *ApJL*, 557, 89

Yuan, W., Brinkmann, W., Siebert, J., & Voges, W. 1998, A&A, 330,
108

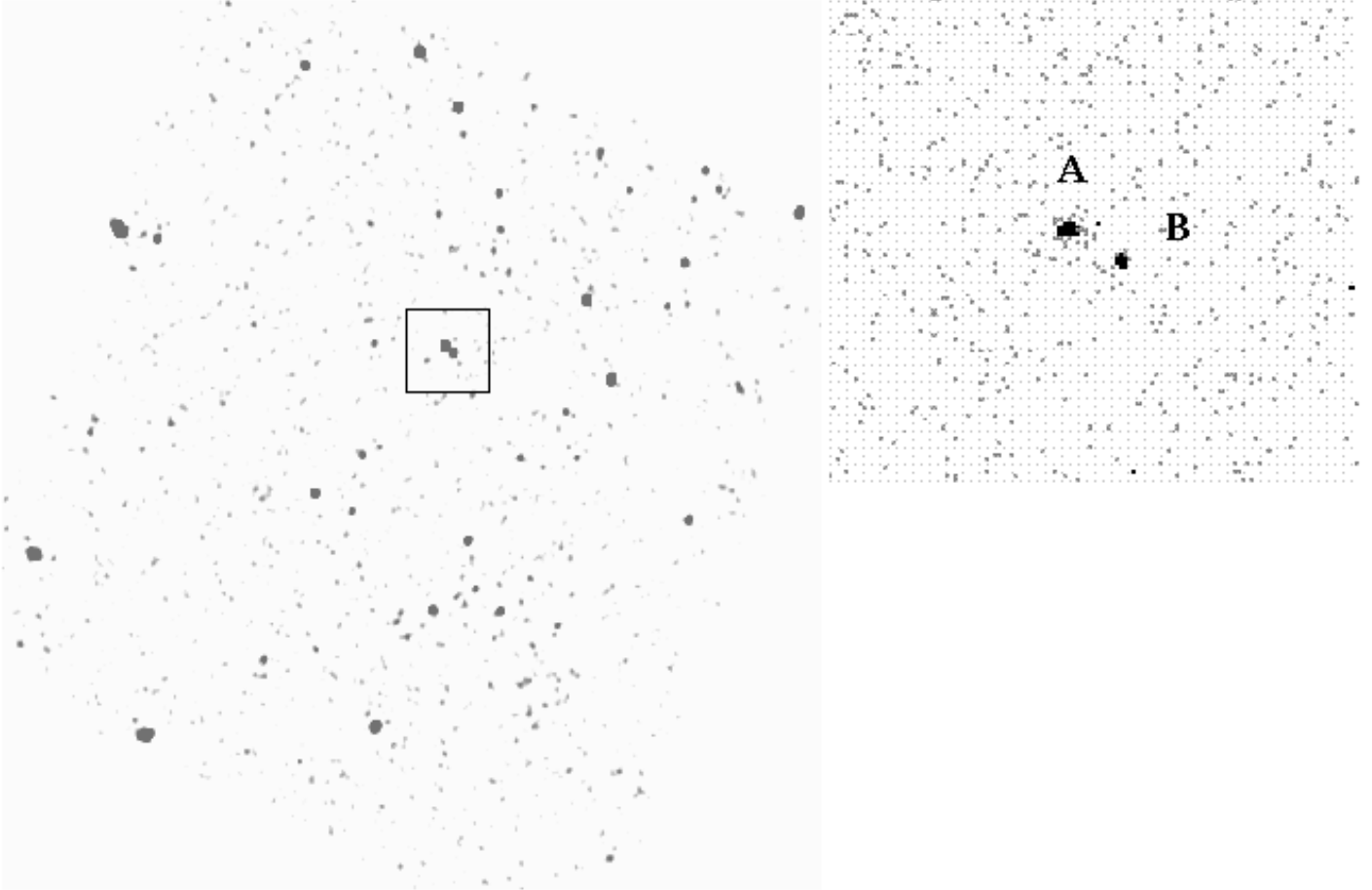


FIG. 1.— LEFT: This $9' \times 9'$ ACIS-S3 (0.3-8keV) image of Q2345+007 (North up, East to the left) was smoothed with a 3 pixel ($1.5''$) gaussian for clarity, and shows the QSO pair on chip S3, about $1'$ North and $30''$ West of the chip center. While numerous point sources are detected, no extended cluster emission is distinguishable around the quasar pair on the image. RIGHT: A $1' \times 1'$ close-up of Q2345+007A,B shows that the pair is well-resolved, with no detectable emission from nearby point sources.

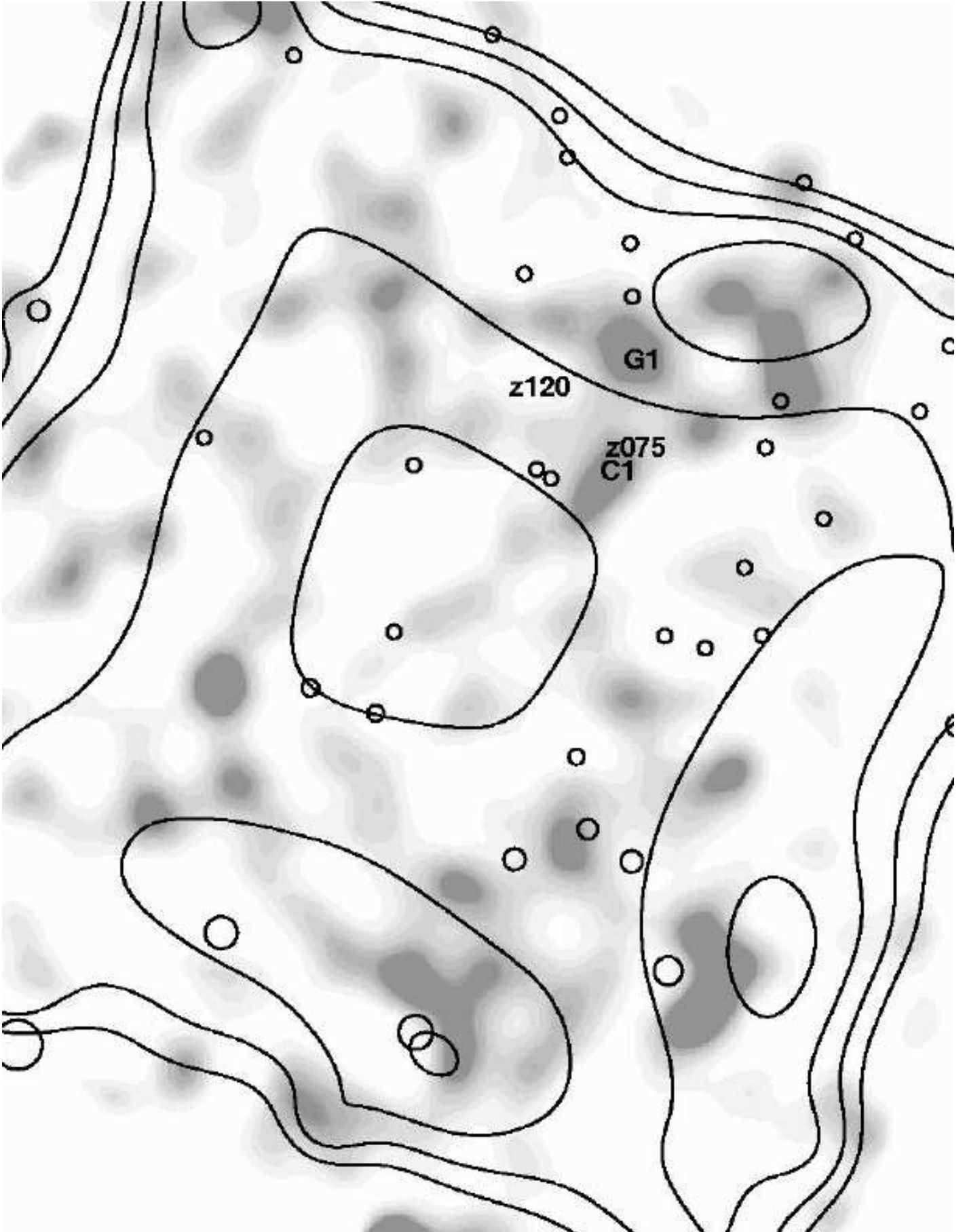


FIG. 2.— Chandra ACIS-S3 Image of the 9.7' field surrounding Q2345+007, with North up, East to the left. We removed counts within these apertures, and then divided by an exposure map before smoothing with a 10'' gaussian. The resulting greyscale shows a mean flux of $\sim 2 \times 10^{-10}$ photons cm^{-2} sec^{-1} $pixel^{-1}$, with values across the image ranging from about 0.7 to 5.3 in those units. Circles with sizes representing the PSF (95% encircled energy) mark the positions of point sources detected by CIAO *wavdetect*. The positions of the twin QSOs are evident just NE of center. The large contours show linear levels (from 500 to 900 cm^2 , in steps of 100) in the exposure map. Positions

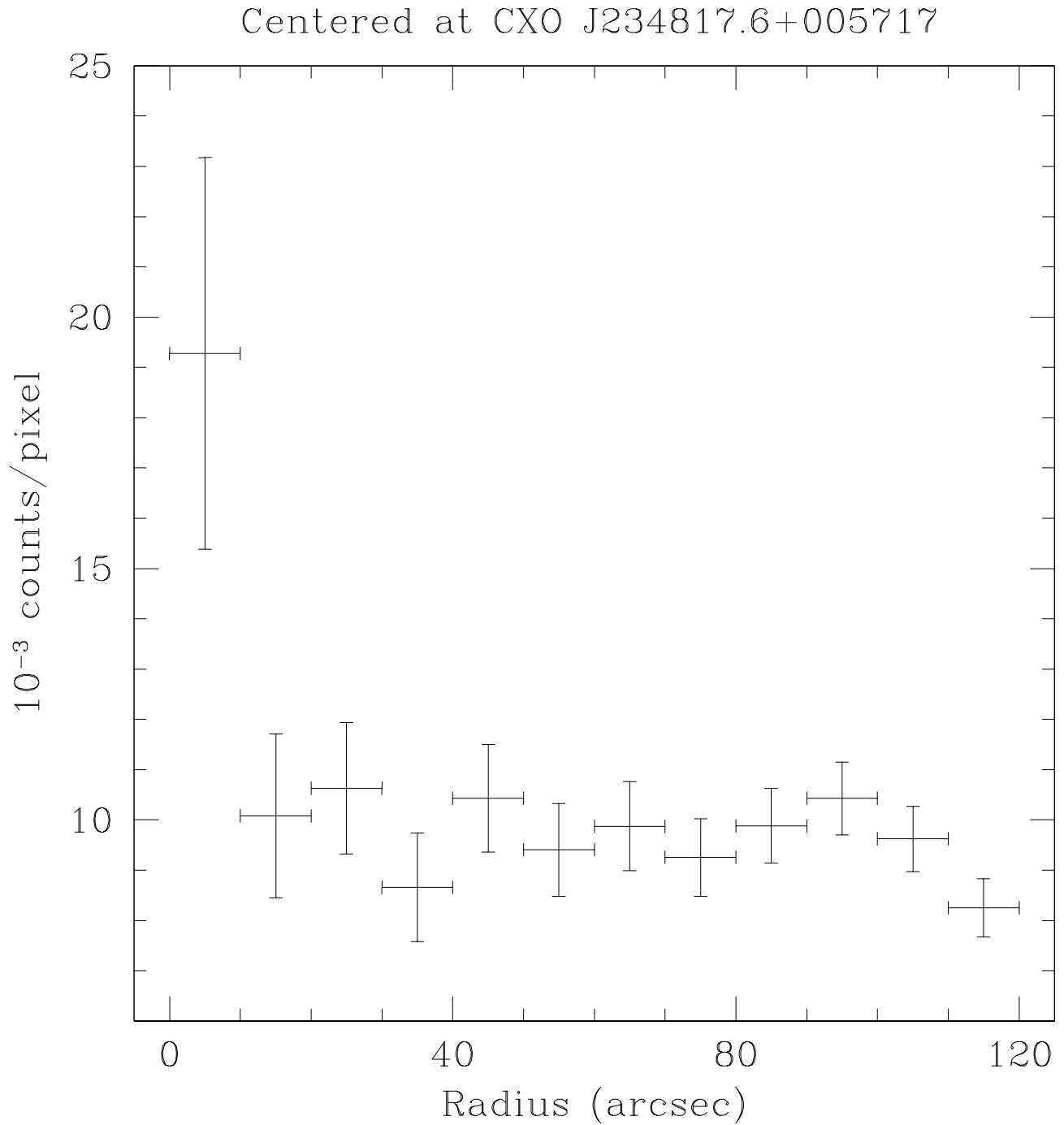


FIG. 3.— This radial profile is centered at the position of CXO J234817.6+005717, the excess nearest the QSOs in Figure 4. We used successive 10'' annuli in a cleaned 0.5-2keV image, excluding both detected point sources and regions with apparent source excesses in Figure 2. Vertical error bars are 1σ , and horizontal bars represent the range of each annulus. The background level (~ 0.01 counts per 0.5'' pixel) has not been subtracted. The profile displays a possible flux excess in the first bin, significant at $2.5\text{-}3\sigma$ above background.

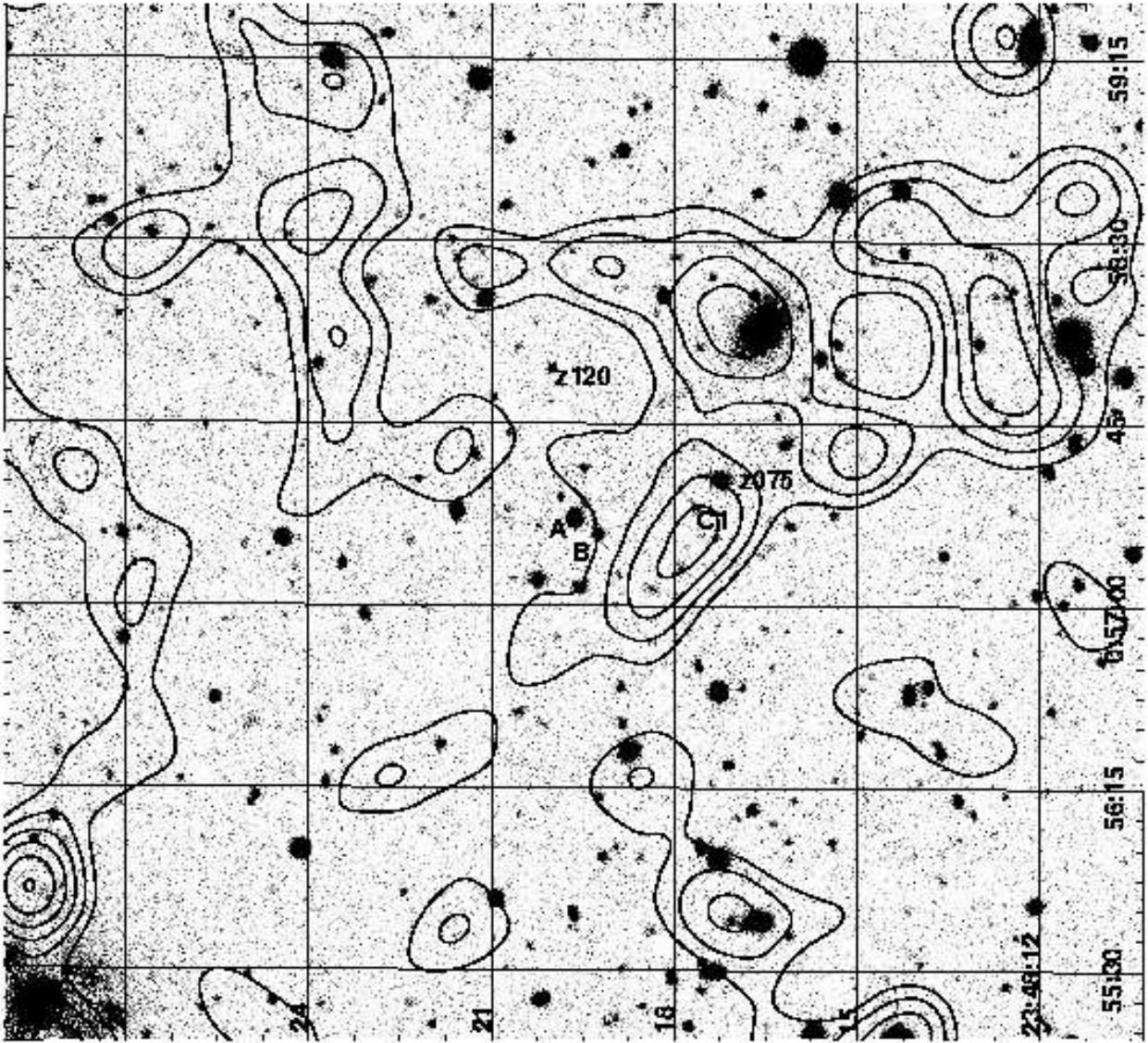


FIG. 4.— An r' image from the CTIO 4meter from UT 29 September 2000 of a $4.25'$ field surrounding Q2345+007. North is up, East to the left, and a J2000 coordinate grid displayed. The large contours show the same X-ray flux levels as in Figure 2. Positions of the QSO images A and B are and of putative optically-identified galaxy clusters are marked in bold type.

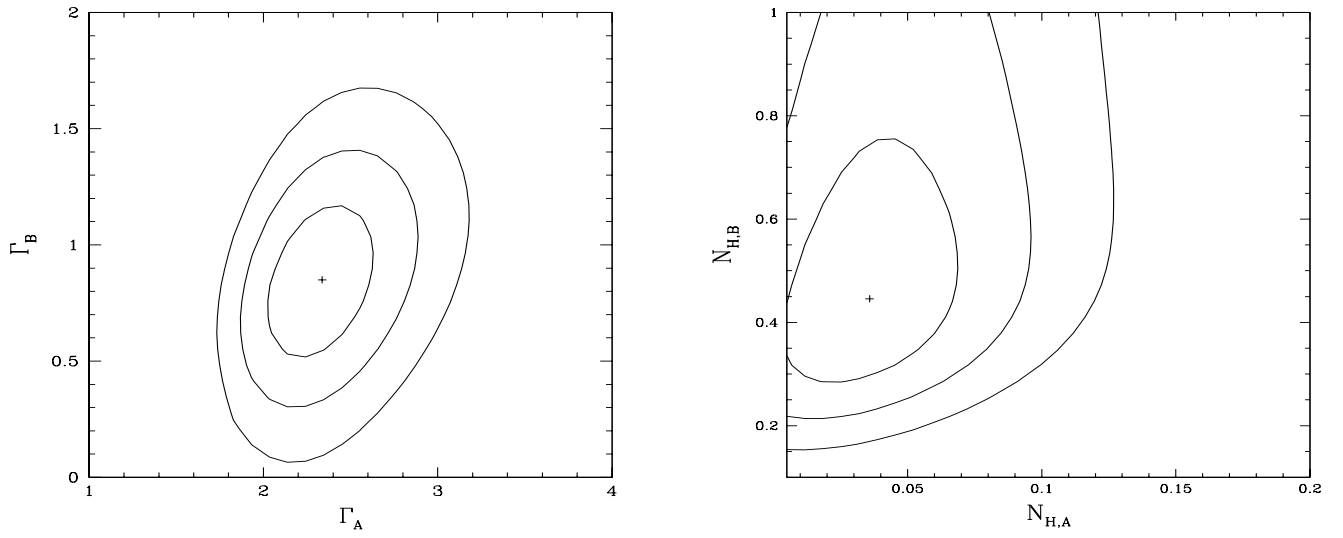


FIG. 5.— Contour plots of confidence levels for simultaneous fits to ACIS spectra of Q2345+007 A and B. The plot at left shows the confidence levels for Γ_A vs. Γ_B in Model (2) where the absorption is assumed to be common. The plot at right shows confidence levels for $N_{H,A}$ vs. $N_{H,B}$ in Model (3) where the power-law slope is assumed to be common.

TABLE 1
MEASURED POSITIONS OF QSOs AND POSSIBLE CLUSTER CENTERS

Center	RA (2000)	Dec ^a	Separation ^b	Reference
Optical				
QSO A,O	23 48 19.6	00 57 21.6	...	1
QSO B,O	23 48 19.2	00 57 17.7	...	1
center	23 48 19.4	00 57 19.2	...	1
C1	23 48 17.2	00 57 22	33	2
G1	23 48 16.5	00 58 08.3	66	2
G2	23 48 17.2	00 57 31.1	36	2
Z075	23 48 16.6	00 57 31	44	3
Z120	23 48 19.3	00 57 57	38	3
X-ray				
QSO A	23 48 19.6	00 57 21.4	0.3	1
QSO B	23 48 19.2	00 57 17.5	0.2	1
CXO J234817.6+005717	23 48 17.6	00 57 17	27	1
CXO J234816.9+005811	23 48 16.9	00 58 11	64	1
CXO J234812.7+005813	23 48 12.7	00 58 13	114	1

^aCoordinates with subarcsecond precision are listed for objects with well-defined centroids from our optical imaging.

^bFor QSOs, separation of X-ray centroids from optical centroids. For putative optical clusters, separations are in arcsec from the center of the QSO pair center.

References. — (1) This paper; (2) Bonnet et al. 1993; (3) Pello et al. 1996.

TABLE 2
MAGNITUDE DIFFERENCES FOR Q2345+007 A AND B

Epoch	Band	$m_B - m_A$	Reference	Epoch	Band	$m_B - m_A$	Reference
1981.92	<i>B</i>	1.43±0.06	5	1991.96	<i>R</i>	1.25±0.09	4
	<i>V</i>	1.43±0.05	5	1992.73	<i>V</i>	1.13±0.12	4
1981.98	<i>r</i>	1.54±0.13	5	1992.88	<i>B</i>	1.30±0.06	4
1982.57	<i>r</i>	1.44±0.15	5	1992.93	<i>K</i>	1.3±0.1	7
1982.90	<i>r</i>	1.41±0.13	5	1993.76	<i>J</i>	1.55	3
1989.65	<i>B</i>	1.30±0.14	6	1993.76	<i>K'</i>	1.51	3
	<i>g</i>	1.31±0.07	6	1998.73	<i>u*</i>	1.62±0.12	8
	<i>r</i>	1.24±0.06	6		<i>g*</i>	1.63±0.03	8
	<i>i</i>	1.08±0.06	6		<i>r*</i>	1.60±0.05	8
1989.67	<i>r</i>	1.28±0.04	6		<i>i*</i>	1.62±0.07	8
1989.69	<i>g</i>	1.32±0.03	6		<i>z*</i>	1.37±0.16	8
	<i>r</i>	1.27±0.04	6	2000.75	<i>g*</i>	1.88±0.01	1
	<i>i</i>	1.19±0.04	6		<i>r*</i>	1.85±0.01	1
1989.96	<i>K</i>	1.11±0.17	4		<i>i*</i>	1.81±0.01	1
1990.79	<i>B_J</i>	1.24	3	2001.63	<i>g*</i>	1.64±0.01	1
1990.79	<i>R</i>	1.19	3		<i>r*</i>	1.65±0.01	1
1990.79	<i>I</i>	1.14	3		<i>i*</i>	1.60±0.01	1

References. — (1) This paper; (2) Bonnet et al. 1993; (3) Pello et al. 1996; (4) Gopal-Krishna et al. 1993; (5) Sol et al. 1984; (6) Weir & Djorgovski 1991; (7) McLeod et al. 1994; (8) SDSS Early Data Release.

Note. — We include only ratios published with accurate dates in *B* band or redder.

TABLE 3
SPECTRAL FIT PARAMETERS

Model	QSO	Γ	N_H (10^{20} cm^{-2})	χ^2 (DOF) ^a
1	A	2.19 ± 0.15	3.8	42.54 (40)
	B	0.79 ± 0.4	...	25.09 (40)
2	A	$2.30^{+0.36}_{-0.30}$	5.3 ± 3.1	67.9 (79)
	B	$0.83^{+0.49}_{-0.44}$
3	A	$2.14^{+0.34}_{-0.28}$	$3.4^{+3.5}_{-2.9}$	65.4 (79)
	B	...	43.9^{+29}_{-18}	...
4	A	$2.23^{+0.33}_{-0.30}$	4.3 ± 3.1	42.77 (39)
	B	$1.37^{+0.79}_{-0.66}$	$23.6^{+28.1}_{-19.2}$	21.32 (39)

Note. — Fit parameters based on simultaneous fitting of spectra using Primini statistics in Sherpa (Freeman et al 2001). Uncertainties are 90% confidence limits. Where no uncertainties are shown, the parameter was frozen at the value displayed. Where only QSO A shows a value, the parameter was fit simultaneously to both components A and B. Models are described in the text.

^a χ^2 based on spectra binned to 10 counts per bin, using given fit parameters.